

1 **The influence of particle composition upon**  
2 **the evolution of urban ultrafine diesel**  
3 **particles on the neighbourhood scale**

4  
5  
6 **Irina Nikolova<sup>1</sup>, Xiaoming Cai<sup>1</sup>, Mohammed Salim Alam<sup>1</sup>,**  
7 **Soheil Zeraati-Rezaei<sup>2</sup>, Jian Zhong<sup>1</sup>, A. Rob MacKenzie<sup>1,3\*</sup>**  
8 **and Roy M. Harrison<sup>1,4</sup>**

9  
10  
11 **<sup>1</sup>School of Geography, Earth and Environmental Sciences**  
12 **University of Birmingham, Edgbaston, Birmingham B15 2TT**  
13 **United Kingdom**

14  
15 **<sup>2</sup>Department of Mechanical Engineering**  
16 **University of Birmingham, Edgbaston, Birmingham B15 2TT**  
17 **United Kingdom**

19 <sup>3</sup>Birmingham Institute of Forest Research (BIFoR)  
20 University of Birmingham, Edgbaston, Birmingham B15 2TT  
21 United Kingdom

22  
23 <sup>4</sup>Also at: Department of Environmental Sciences / Center of  
24 Excellence in Environmental Studies, King Abdulaziz University,  
25 PO Box 80203, Jeddah, 21589, Saudi Arabia

26  
27 \* Corresponding author: [a.r.mackenzie@bham.ac.uk](mailto:a.r.mackenzie@bham.ac.uk)

28  
29  
30  
31  
32  
33  
34  
35  
36  
37  
38  
39  
40  
41  
42  
43  
4  
3

**ABSTRACT**

A recent study demonstrated that diesel particles in urban air undergo evaporative shrinkage when advected to a cleaner atmosphere (Harrison et al., Atmospheric Environment, 2016, 125, 1-7). We explore, in a structured and systematic way, the sensitivity of nucleation-mode diesel

44 particles (diameter < 30 nm) to changes in particle composition and saturation vapour  
45 pressure. We use a multi-component aerosol microphysics model based on surrogate molecule  
46 ( $C_{16}$ - $C_{32}$  n-alkane) volatilities. For standard atmospheric conditions (298 K, 1013.25hPa), and  
47 over timescales (ca. 100 s) relevant for dispersion on the neighbourhood scale (up to 1 km), the  
48 choice of a particular vapour pressure dataset changes the range of compounds that are  
49 appreciably volatile by 2-6 carbon numbers. The nucleation-mode peak diameter, after 100 s of  
50 model runtime, is sensitive to the vapour pressure parameterisations for particles with  
51 compositions centred on surrogate molecules between  $C_{22}H_{46}$  and  $C_{24}H_{50}$ . The vapour pressure  
52 range is between  $9.23 \times 10^{-3}$  and  $8.94 \times 10^{-6}$  Pa for  $C_{22}H_{46}$  and  $2.26 \times 10^{-3}$  and  $2.46 \times 10^{-7}$  Pa for  $C_{24}H_{50}$ .  
53 The vapour pressures of components in this range are therefore critical for the modelling of  
54 nucleation-mode aerosol dynamics on the neighbourhood scale and need to be better  
55 constrained. Laboratory studies have shown this carbon number fraction to derive  
56 predominantly from engine lubricating oil. The accuracy of vapour pressure data for other  
57 (more and less volatile) components from laboratory experiments, is less critical. The influence  
58 of a core of non-volatile material is also considered.

59

60 The new findings of this study may also be used to identify the Semi-Volatile Organic Compound  
61 (SVOC) compositions that play dominating roles in the evaporative shrinkage of the nucleation  
62 mode observed in field measurements (Dall'Osto, et al., Atmospheric Chemistry & Physics, 2011,  
63 11, 6623-6637).

65 Ultrafine particles (UFP, with particle diameter  $D_p < 100$  nm) have been increasingly a focus of  
66 urban air research over the last two decades. The main source of UFP in outdoor urban air is  
67 typically road traffic (Kumar et al., 2014). Harrison et al. (2011) reported that on a busy highway  
68 in central London, UK, 71.9% of particles by number were traffic-generated; of which 27.4% are  
69 found in the semi-volatile exhaust nucleation mode (size between 15 and 30 nm), 38% are in the  
70 exhaust solid mode (size  $> 30$  nm) and the remaining 6.5% are from brake dust and  
71 resuspension (size  $> 2000$  nm). Hereafter, nucleation mode particles are defined as particles  
72 with diameter less than 30 nm, Aitken mode particles have a diameter in the range 30 – 100 nm.  
73 The proximity of the UFP traffic source to the public, and the large number of UFP emitted by  
74 traffic, have prompted health-related research that has accrued evidence pointing to the  
75 toxicity and potentially harmful effects of UFP on human health (Atkinson et al., 2010).  
76 Experimental and modelling studies have advanced our understanding of the behaviour of  
77 urban air UFP, e.g. the relevant aerosol dynamics important to the evolution of the UFP in space  
78 and time (Jacobson, 2005; Allen et al., 2007; Biswas et al., 2007; Dall'Osto et al., 2011; Nikolova  
79 et al., 2011; Karnezi et al, 2014, Karl et al., 2016 ).

80

81 Nonetheless, key information regarding the size-resolved composition of the UFP is missing,  
82 which limits our ability to determine the impact of gas-transfer processes on UFP evolution.  
83 Progress has been made in modelling traffic-generated particles (including the ultrafine fraction)  
84 using a volatility basis set, defined using the effective saturation concentration (Donahue et al.,  
85 2006). Progress in identifying the precise chemical composition of traffic-generated particles has  
86 been made by resolving the so-called 'unresolved complex mixture' (largely uncharacterised  
87 organics in traditional gas chromatography) via two-dimensional gas chromatography (GC×GC;  
88 Chan et al., 2013). Alam et al. (2016) show that emitted ultrafine diesel particles consist of a  
89 substantial amount of organic material from both unburnt diesel fuel and engine  
90 lubricating oil. They attribute the low molecular weight Semi-Volatile Organic Compounds

7

8

91 (SVOCs, having carbon number < 18) predominantly to the unburnt diesel fuel, whereas heavier  
92 SVOCs (carbon number > 18) are attributed predominantly to the engine lubricating oil. A typical  
93 GC×GC separation is shown in the chromatogram (Figure 1) for diesel engine exhaust emissions  
94 in the particulate-phase Aitken mode ( $56 < D_p < 100$  nm). Compounds are separated by  
95 volatility along the *x*-axis (first separation dimension) and by polarity in the *y*-axis (second  
96 dimension). Peak identification is based on retention indices and mass spectral data from the  
97 National Institute of Standards and Technology (NIST) library. The majority of chromatography  
98 peaks (identified as aliphatic alkanes, lower black polygons) are present between  $C_{18}$  to  $C_{26}$ ,  
99 corresponding to the compounds identified in the engine lubricating oil and particulate phase  
100 engine emissions (Alam et al. 2017). Bar charts above the chromatogram show the volatility  
101 distribution of total alkanes (red) and total identified compounds (black), indicating that,  
102 although many hundreds of individual chemical compounds are detected, the majority of the  
103 SVOCs emissions consist of alkanes. Both the alkane composition and the total composition  
104 distributions show a broad peak centred at  $C_{25}$ .

105

106 Most primary organic particle emissions are semi-volatile in nature and thus they are likely to  
107 evaporate with atmospheric dilution and moving away from the source (Robinson et al., 2007).  
108 This has been observed by Dall'Osto et al. (2011; see also Figure 1- S in Supplementary  
109 Information) as part of the REPARTEE campaign (Harrison et al., 2012). Dall'Osto et al. (2011)  
110 reported a remarkable decrease in the measured nucleation-mode peak particle diameter  
111 ( $D_{pg,nuc}$ ) between a street canyon ( $D_{pg,nuc} = 23$  nm) and the downwind neighbourhood ( $D_{pg,nuc} = 8$ -  
112 9 nm) ca. 650 m distant in central London (UK). The travel time, depending on the wind speed,  
113 can vary from ~100 s to ~ 300 s. Nucleation formation of new particles in the atmosphere was  
114 ruled out as a possible reason for the observed behaviour. Instead, the decrease in particle  
115 diameter was attributed to the effect of evaporation and substantial mass loss from the particle  
116 surface (hereafter referred to as REPARTEE-like aerosol dynamics). Alam et al. (2016) present  
117 the composition of diesel UFP particles measured on a laboratory test-rig (cf. Figure 2-S in

118 Supplementary Information), however the range of variability of the particle composition in  
119 emissions is still unknown. It is also not known how the organic material is distributed onto the  
120 nucleation and Aitken modes of the UFP distribution in the atmosphere.

121  
122 Numerical experiments can test the plausibility of possible missing components of the system,  
123 and can advise on which experimental studies will be most likely to resolve the existing  
124 knowledge gaps. Nikolova et al. (2016) describe a modelling framework that can produce  
125 nucleation-mode dynamics consistent with observations. However, missing in that study is the  
126 identification of critical thermodynamic parameters and size-resolved composition that could  
127 determine or point to a REPARTEE-like aerosol dynamics.

128  
129 In the present study, we develop a method to search the particle composition space — i.e. the  
130 volatility parameter space — to identify a group of surrogate n-alkanes in the  $C_{16}H_{34}$ - $C_{32}H_{66}$   
131 range that could explain a decrease in the nucleation-mode particle diameter to 10 nm or below  
132 as seen in the measurements in London (Dall'Osto et al., 2011). The model simulations are  
133 focused on events after dilution and cooling of the exhaust-pipe plume. We provide a more  
134 robust approach to identify crucial parameters responsible for the UFP behaviour in the  
135 atmosphere on the neighbourhood scale including the identification of parameter sets that are  
136 incompatible with the observed behaviour in urban air of nucleation mode UFP. We describe a  
137 new way to simulate and evaluate the role of the SVOCs composition on the atmospheric  
138 behaviour of the size-resolved urban UFP and examine more complex sets of composition  
139 involving a non-volatile core. We also assess the critical role of saturation vapour pressure on  
140 the size-resolved aerosol dynamics.

141  
142 In this study we use Lagrangian box-model simulations of the evolution of urban ultrafine diesel  
143 particles on the neighbourhood scale (up to 1 km). Key results will be presented and discussed  
144 in the main text; more details are provided in the Supplementary Information. The Methodology

145 section describes the modelling approach. The Results section presents the model output. In the  
146 Discussion and Conclusions sections, the key findings are summarised with suggestions for  
147 further work.

148

## 149 **2. METHODOLOGY**

150 We adopt a 'surrogate molecule' approach to UFP composition, based on the chemical  
151 speciation shown in analyses such as Figure 1. The composition of UFP is simulated as  
152 comprising n-alkanes from  $C_{16}H_{34}$  to  $C_{32}H_{66}$ , which are the most abundant compounds in Figure  
153 1. Previously (Nikolova et al., 2016), we initialised the n-alkane abundance in gas and particle  
154 phases using roadside and urban background observations in Birmingham, U.K. (Harrad et al.,  
155 2003). In what follows, we retain this roadside gas-phase initialisation (see below), but choose a  
156 more general method for initialising the particle composition, in order to test the sensitivity of  
157 the results to the initialisation in a systematic way. By adopting a surrogate molecule approach,  
158 we are effectively anchoring the model volatility basis set in physico-chemical data, as discussed  
159 further below.

160

161 The SVOC mass fractions in a particle are represented by a truncated Gaussian distribution that  
162 is centred for each model run at a given n-alkane in the range from  $C_{16}H_{34}$  to  $C_{32}H_{66}$  with a  
163 standard deviation,  $\sigma$ , varying from 1 to 5. Below we call the surrogate n-alkane on which the  
164 composition distribution is centred, the *modal composition*. Example compositions are shown in  
165 Figure 2 for a Gaussian distribution centred at  $C_{24}H_{50}$ . A narrower mass distribution, with  $\sigma = 1$ ,  
166 focuses predominantly (ca. 40%) on the component,  $j$  ( $C_{24}H_{50}$ ), at which the distribution is  
167 centred, with a smaller (ca. 24%) contribution from the adjacent compounds  $C_{23}H_{48}$  and  $C_{25}H_{52}$ ,  
168 and a minor contribution (ca. 5%) from  $C_{22}H_{46}$  and  $C_{26}H_{54}$ . The contribution of the remaining  
169 compounds from the tail of the distribution is very low and less than 1%. However, a wider mass  
170 distribution (e.g.  $\sigma = 5$ ) approximates a flat distribution and includes a contribution from the  
171 majority or all of the compounds in the n-alkane range  $C_{16}H_{34}$ - $C_{32}H_{66}$ . Monotonically decreasing

13

14

172 distributions occur for distributions centred at either end of the C<sub>16</sub>H<sub>34</sub>-C<sub>32</sub>H<sub>66</sub> range. Overall, if  
173 one excludes the compounds with less than 1% contribution, modal compositions centred at  
174 carbon number,  $j$ , with  $\sigma = 1, 2, 3, 4, \& 5$ , contain surrogate compounds  $\pm 2, 4, 7, 9, \& 11$   
175 carbon numbers of  $j$  (formally, to remain in the 16-32 carbon number range,  $[\max(16, j-$   
176  $2):\min(32, j+2)]$ ,  $[\max(16, j-4):\min(32, j+4)]$ ,  $[\max(16, j-7):\min(32, j+7)]$ ,  $[\max(16, j-9):\min(32,$   
177  $j+9)]$ , &  $[\max(16, j-11):\min(32, j+11)]$ ), respectively. Multi-modal compositions, or others  
178 differing strongly from Gaussian, are not investigated in the present study, but could be  
179 accommodated by a simple extension of the method.

180

181 We use a Gaussian distribution to represent the composition of the particles because it provides  
182 a structured and systematic way to evaluate the organic-aerosol phase partitioning and the  
183 amount of organic matter in the UFP. This is important for the behaviour and evolution of the  
184 UFP at various timescales relevant for the urban atmosphere. Although there is no reason to  
185 discount other functional forms for the composition distribution (e.g., skew Gaussian, log-  
186 normal, Pareto, linear, etc), the Gaussian distributions chosen represent a simple two-  
187 parameter approach to explore the volatility/composition space available.

188

## 189 **2.1 Box Model**

190 The model used in this study is the UFP version (Nikolova et al., 2016) of CiTTy-Street (Pugh et  
191 al., 2012); that is, a box-model configuration that accounts for the multicomponent nature of  
192 the urban ultrafine particles. The CiTTy-Street-UFP model is used with 15 discrete size bins, with  
193 an initial diameter range between 5.8-578 nm in a uniform log-scale. The model can operate in  
194 two modes with respect to the aerosol dynamics: Eulerian (fixed particle-diameter grid) or  
195 Lagrangian (moving particle-diameter grid). The Eulerian mode is selected when the UFP size  
196 distribution is evaluated in the presence of emissions and exchange of particles between boxes  
197 (Nikolova et al., 2016). The Lagrangian mode can be selected when the UFP size distribution is  
198 evaluated for an isolated air parcel, i.e., when no emissions or transport between boxes are

15

16



199 present. In this study, the Lagrangian mode is selected in a zero-dimensional configuration with  
200 no emissions or transport in/out of the box. The UFP dynamics (only condensation/evaporation)  
201 are simulated such that particles are allowed to grow/shrink to their exact size without any  
202 redistribution onto fixed bins in a grid with bin bounds left open in a fully moving diameter  
203 scheme (see, for example, Jacobson et al., 1997). Our earlier work (Nikolova et al., 2016) has  
204 shown that deposition and coagulation have a minor effect in the current scenario and so were  
205 switched off to allow a more straightforward diagnosis of model behaviour. The  
206 condensation/evaporation process applies Raoult's Law (for an ideal solution of the volatile  
207 compounds) and a mass accommodation coefficient  $\alpha = 1$  (Julin et al., 2014) for all SVOC. The  
208 Kelvin effect is also considered, which alters the saturation vapour pressure of the compounds  
209 as a function of the particle diameter, the surface tension of the SVOC mixture/solution, and the  
210 molecular weight of the participating compounds. The Kelvin effect is pronounced for particles  
211 with a diameter less than 20 nm and substantial for particles with diameter less than 10 nm. The  
212 Kelvin term accelerates the evaporation for all compounds under consideration in this study and  
213 more notably for the high-molecular-weight compounds due to their larger molar volume.  
214 The model results are evaluated at 1, 10 and 100 s. The timescale of 100 s is based on estimate  
215 of the travel time on the neighbourhood scale (i.e., horizontal travel distances  $\ll 1$  km).

## 216 **2.2 Modal Composition and Initial Size-Resolved UFP distribution**

217 The initial size-resolved UFP distribution is based on the measurements of Dall'Osto et al. (2011)  
218 and reproduced in Figure 1-S in the Supplementary Information. This ultrafine size distribution  
219 represents the typical street canyon bimodal size distribution found next to a traffic site, e.g.  
220 next to Marylebone Road in London (UK). The distribution has a well-defined nucleation mode  
221 with a peak number concentration at  $D_{pg,nuc} \sim 23\text{-}24$  nm. The Aitken mode appears as a shoulder  
222 attached to the nucleation mode with a peak number concentration found at  $D_{pg,aim}$  between  
223 50-60 nm.

224 The initial UFP size-resolved composition is represented by modal compositions in the range  
225  $C_{16}H_{34}\text{-}C_{32}H_{66}$ , as detailed above, and a standard deviation  $\sigma$  from 1 to 5. A non-volatile core is

226 included in the ultrafine particles. While studies broadly agree on the existence of a non-volatile  
227 core in the Aitken mode (Biswas et al., 2007; Wehner et al., 2004; Ronkko et al., 2013), it is  
228 unclear if nucleation-mode particles contain some non-volatile material or if they are entirely  
229 composed of (semi-)volatile SVOC. We have tested the sensitivity to the existence of non-  
230 volatile material in the nucleation mode particles by initialising with 1%, 5% or 10% by mass  
231 non-volatile material for each modal composition (see Supplementary Information for details of  
232 the initialisation); results are discussed later in this paper. Simulations are performed by  
233 considering the initialised Aitken mode predominantly non-volatile and coated only with 10%  
234 volatile material. This is based on the observations during the REPARTEE campaign (Harrison et  
235 al., 2012) that show a fairly stable Aitken mode between the street canyon and the  
236 neighbourhood. The initial size-resolved modal compositions, composition standard deviations  
237 and non-volatile core in the nucleation and Aitken modes are detailed in Tables 1-S, 2-S, 3-S and  
238 4-S in the Supplementary Information. We also provide information on the input parameters of  
239 the log-normal UFP size distribution for Nucleation and Aitken modes.

240

### 241 **2.3 Saturation Vapour Pressures and Gas-Phase Concentrations**

242 The driving force for condensation/evaporation is the difference between the partial pressure of  
243 each representative SVOC and its saturation vapour pressure (hereafter vapour pressure) over  
244 the ideal solution in the nucleation mode condensed phase. Figure 3 shows vapour pressures  
245 above pure, flat, supercooled liquids for n-alkanes in the range  $C_{16}H_{34}$ - $C_{32}H_{66}$ , following Chickos  
246 and Lipkind (2008), Compernelle et al. (2011), Lemmon and Goodwin (2000), the Epi Suite  
247 calculator (US EPA, 2017), and the UmanSysProp tool (Topping et al., 2016). The UmanSysProp  
248 tool provides vapour pressure data based on the work of Nannoolal et al. (2008) and Myrdal and  
249 Yalkowsky (1997) with the boiling points of Joback and Reid (1987), Stein and Brown (1994), and  
250 Nannoolal et al. (2004). There is a very substantial range of estimated vapour pressures for the  
251 same compounds in Figure 3, especially for the high molecular weight n-alkanes. The reported  
252 data agrees within an order of magnitude between  $C_{16}H_{34}$  and  $C_{19}H_{40}$ , but discrepancies of much

19  
20

253 more than an order of magnitude are evident for the high molecular weight compounds. The  
254 vapour pressure ranges of  $C_{22}H_{46}$  and  $C_{24}H_{50}$  are between [ $9.23 \times 10^{-3}$  and  $8.94 \times 10^{-6}$  Pa] and  
255 [ $2.26 \times 10^{-3}$  and  $2.46 \times 10^{-7}$  Pa], respectively. An enormous difference in the vapour pressure for  
256  $C_{32}H_{66}$  (from  $2.66 \times 10^{-5}$  Pa in Epi Suite, to  $3.20 \times 10^{-15}$  Pa in Nannoolal et al., 2008 with the boiling  
257 point of Joback and Reid, 1987, called A-a hereafter) is clearly seen in Figure 3. Epi Suite (U.S.  
258 Environmental Protection Agency) provides the highest vapour pressures for all selected species  
259 in comparison with the rest of the data. Nannoolal et al. (2008) and Myrdal-Yalkowsky (1997)  
260 data, both using the boiling point of Joback and Reid (1987), provide similar results and present  
261 the lowest vapour pressures among the selected n-alkanes. For the purpose of our sensitivity  
262 study, three representative datasets are nominated as input, namely: Myrdal-Yalkowsky (1997)  
263 with the boiling point of Nannoolal et al. (2004, called B-c in Figure 3 and hereafter);  
264 Compernelle et al. (2011, called Co); and A-a. Hereafter we use the legend abbreviations in  
265 Figure 3 when referring to these selected vapour pressures, which are towards the upper, mid-  
266 and lower end of the reported data. The vapour pressure from the EPI Suite calculator has been  
267 omitted from the analysis below because it has been considered in our previous study (Nikolova  
268 et al., 2016).

269

270 The gas-phase concentration in the box is initialised with measured gas-phase concentrations in  
271 the  $C_{16}H_{34}$ - $C_{32}H_{66}$  range from a traffic site (Harrad et al., 2003) and reported in Table 6-S in the  
272 Supplementary Information. For hydroxyl (OH) radical concentration  $\sim 10^6$  molec  $cm^{-3}$ , the  
273 timescale for atmospheric oxidation of  $C_{16}H_{34}$  is about  $10^6$  s (Atkinson and Arey, 2003).  
274 Therefore oxidation of SVOC is neglected given the timescale in our study (100 s). The urban  
275 background gas-phase concentration is kept at zero. All model simulations are run at 298 K; the  
276 effects of temperature on vapour pressure differences as a function of carbon number are  
277 discussed in the Supplementary Information.

278

279 We have performed a total of (17 modal compositions) x (5  $\sigma$  values) x (3 non-volatile core

21  
22

280 amounts) x (3 vapour pressures) = 765 model runs to explore the sensitivity of particle dynamics  
281 on the neighbourhood scale.  
282  
283 The Supplementary Information contains information regarding the initial size distribution,  
284 modal composition in the nucleation and Aitken modes, and gas-phase concentrations.  
285 Accumulation-mode aerosol (particles diameter  $D_p > 100$  nm) is not considered in this study.  
286 Accumulation-mode particles have much smaller number concentrations than the nucleation  
287 and Aitken modes in polluted urban areas, and are influenced by aging and transport over larger  
288 scales.

289

### 290 **3. RESULTS**

#### 291 **3.1 Effect of composition on Nucleation-Mode Peak Diameter**

292 We consider first model runs in which the vapour pressure data follows Co (Compernelle et al.  
293 (2011)) and nucleation mode particles initialised with 1% non-volatile material. The nucleation  
294 mode peak diameter  $D_{pg,nuc}$  is evaluated at 1 s and 100 s of model run-time in runs with varying  
295 modal composition and composition standard deviations. Figure 4 shows  $D_{pg,nuc}$  (y-axis) at 1s  
296 simulation time, for each model run, plotted with respect to the modal composition and  
297 composition standard deviation,  $\sigma$ .

298

299 Figure 4 maps out the effect of nucleation-mode composition at this very early stage in the  
300 model simulation. For example, at  $\sigma = 1$  and initial mass distribution centred at  $C_{20}H_{42}$  (green  
301 solid line with a square marker), the  $D_{pg,nuc}$  decreased from 23 nm (initial diameter at  $t = 0$  s) to  
302 12 nm in one second due to evaporation of volatile material from the particles. At  $\sigma = 2$ ,  $D_{pg,nuc} =$   
303 15 nm, a somewhat larger diameter than for  $\sigma = 1$ , due to the inclusion of material of lesser  
304 volatility in the particle composition and, hence, a decrease in evaporation overall. For modal  
305 compositions between  $C_{16}H_{34}$  and  $C_{20}H_{44}$ , an increase in  $\sigma$  leads to a pronounced deceleration in  
306 overall evaporation and, hence, a much larger nucleation mode peak diameter at 1 s simulation

23

24

307 time. The opposite effect occurs for modal compositions of  $C_{22}H_{46}$  and above, i.e. increasing  $\sigma$   
308 for a given modal composition decreases  $D_{pg,nuc}$  at 1 s. This is due to the addition of quickly  
309 evaporating lower molecular weight n-alkanes.

310

311 For a modal composition of  $C_{21}H_{44}$ , increasing  $\sigma$  makes almost no difference to the model  
312 outcome at 1 s. Below, we call the modal composition that shows insensitivity to  $\sigma$  for a given  
313 model output time, the *threshold modal composition*. The threshold modal composition points  
314 to the composition compound that is in equilibrium between gas and particulate phases for the  
315 selected timescale. Lower-carbon-number compositions than the threshold modal composition  
316 evaporate quicker and therefore have reached equilibrium with their respective gas  
317 concentrations on a much shorter timescale. The higher-carbon-number compositions  
318 evaporate slowly and are out-of-equilibrium with their respective gas concentrations for the  
319 selected timescale.

320

321 The model output time of 1 s corresponds to the evaporation timescale of  $C_{21}H_{44}$  under the  
322 current model setting, in analogy to the e-folding time for an exponentially decaying process.  
323 That is, at this time, a significant proportion (e.g.  $1-e^{-1} \sim 63\%$  for one e-folding time, and  $1-e^{-2} \sim$   
324  $86\%$  for two e-folding times) of the initial mass has been evaporated. Furthermore, the  
325 timescales are much shorter for those lower than  $C_{21}H_{44}$  carbon-number compositions (e.g.  
326  $C_{20}H_{42}$ ,  $C_{19}H_{40}$ , ...) and much longer for those higher than  $C_{21}H_{44}$  carbon-number compositions  
327 (e.g.  $C_{22}H_{46}$ ,  $C_{23}H_{48}$ ,...).

328

329 To continue the previous example of the modal composition of  $C_{20}H_{42}$ , the case with  $\sigma = 2$   
330 includes not only less volatile materials (i.e. higher-carbon-number SVOCs), but also an equal  
331 amount of more volatile materials (i.e. lower-carbon-number SVOCs), as indicated by Figure 2.  
332 One might suppose that inclusion of the more volatile material would balance the effect of  
333 including less volatile materials. However, following our argument above, most of the lower-

25

26

334 carbon-number compounds including  $C_{20}H_{42}$  will have evaporated before the given time of 1 s  
335 due to their having much shorter evaporation timescales than  $C_{21}H_{44}$ . Thus any material  
336 repartitioned from  $C_{20}H_{42}$  to the lower-carbon-number compounds, in changing the model  
337 settings from  $\sigma = 1$  to  $\sigma = 2$ , will not alter the total amount of evaporation and thus the  
338 shrinkage rate.

339

340 To take a second example: for  $C_{22}H_{46}$ , any material reallocated from  $C_{22}H_{46}$  to the higher-carbon-  
341 number compounds (due to changing the model setting from  $\sigma = 1$  to  $\sigma = 2$ ) will contribute  
342 negligibly to the shrinkage simply because the evaporation timescales for those higher-carbon-  
343 number components are much longer than 1 s, whilst the materials repartitioned from  $C_{22}H_{46}$  to  
344 the lower-carbon compounds will contribute significantly to evaporation in the first second of  
345 model run-time, causing the decreasing trend of the curve shown in Figure 4.

346

347 One implication of this finding is that, if a timescale of 1 s is of interest, the aerosol dynamics of  
348 the system is dominated by the threshold modal composition of  $C_{21}H_{44}$ . Those lower-carbon-  
349 number compositions evaporate in less than 1 s and are approximately in equilibrium with their  
350 respective gas concentrations in the environment. The higher-carbon-number compositions  
351 evaporate slowly and at this time of 1 s, only a small or a negligible proportion has been  
352 evaporated. A few compositions with highest carbon numbers (e.g.  $C_{31}H_{64}$ ,  $C_{32}H_{66}$ ) have  
353 evaporated almost nothing. Therefore these compositions are effectively non-volatile for these  
354 conditions.

355

356 Nucleation-mode particles have an initial non-volatile mass of  $2.9 \text{ ng m}^{-3}$ . Modal compositions  
357 from  $C_{16}H_{34}$  to  $C_{19}H_{40}$  and  $\sigma = 1$  will lose all their volatile mass in 1 s (Table 1). The initial  $D_{pg,nuc}$   
358 decreases from 23 nm to 9 nm and no volatile material is present, i.e. particles are composed of  
359 non-volatile core only. Little or no change is simulated in terms of mass and diameter for modal  
360 composition  $C_{32}H_{66}$ .

27

28

361

362 At 100 s, the evaporation of existing mass from the surface of the particles is evident also for  
363 higher molecular weight components (Table 1). The  $D_{pg,nuc}$  at 100 s is plotted in Figure 5. The  
364 diameter has further decreased with a more pronounced drop for all  $\sigma$  and modal compositions  
365 up to  $C_{25}H_{52}$ .  $C_{25}H_{52}$  is, therefore, the threshold modal composition at this model output time.

366

367 The horizontal line drawn at 10nm on Figure 5 corresponds to evaporation approximating  
368 REPARTEE-like behaviour. At  $\sigma = 1$ , modal compositions in the range  $C_{16}H_{34}$ - $C_{23}H_{48}$  — and vapour  
369 pressures and gas-phase partial pressures as detailed in the methodology — could plausibly  
370 explain a particle diameter decrease from 23 nm to  $\sim 9$  nm. Such a narrow range of surrogate  
371 molecular compounds is incompatible with experimental observations such as Figure 1. At  $\sigma = 2$   
372 and  $\sigma = 3$ , modal compositions from  $C_{16}H_{34}$  up to  $C_{22}H_{46}$  and  $C_{21}H_{44}$ , respectively, can plausibly  
373 approximate REPARTEE-like behaviour. At  $\sigma = 4$  and  $\sigma = 5$  modal compositions from  $C_{16}H_{34}$  up to  
374  $C_{19}H_{40}$  and  $C_{17}H_{36}$ , respectively, plausibly simulate REPARTEE-like behaviour.

375

### 376 **3.2 Effect of Vapour Pressure on the Nucleation-Mode Peak Diameter**

377 We compare the simulated nucleation-mode peak diameter,  $D_{pg,nuc}$ , at 100 s using the vapour  
378 pressure parameterisations B-c, Co and A-a (cf. Figure 3). The nucleation mode particles are  
379 initialised with 1% non-volatile material in these simulations. Diameter change when using Co  
380 vapour pressure has been discussed in the previous section. The values of vapour pressure in  
381 the Co data are intermediate between the B-c and A-a data. Hence,  $D_{pg,nuc}$  at 100 s using vapour  
382 pressure parameterisations A-a and B-c (see Supplementary Information), as expected, shows  
383 the same general behaviour as for vapour pressure parameterisation Co, but with a marked  
384 change in threshold modal composition. In order of decreasing vapour pressure (Figure 3), the  
385 threshold modal composition value changes from  $C_{27}H_{56}$  for the B-c parameterisation (Figure 4-S  
386 in the Supplementary Information), to  $C_{25}H_{52}$  for Co (Figure 5), to  $C_{22}H_{46}$  for A-a (Figure 5-S in the  
387 Supplementary Information). We restrict ourselves to integer values of threshold modal

29

30

388 composition to maintain a straightforward connection back to the homologous chemical series  
389 in Figure 1, although there is nothing in principle to prevent us from attributing real number  
390 values to the threshold modal composition.

391

392 There is no composition with  $\sigma = 4$  and  $\sigma = 5$ , at the lower volatility A-a vapour pressure  
393 parameterisation, that produces REPARTEE-like behaviour; i.e., decrease of the nucleation-  
394 mode peak diameter from 23 nm to 10 nm or below. At  $\sigma = 5$ , the nucleation-mode particles can  
395 lose a maximum of  $\sim 9$  nm of their initial diameter for modal composition  $C_{16}H_{34}$  (please refer to  
396 Figure 5-S in the Supplementary Information). Little or no change in mode diameter is simulated  
397 for modal compositions between  $C_{24}H_{50}$  and  $C_{32}H_{66}$  and  $\sigma = 1$ , indicating that these combinations  
398 of composition and vapour pressure parameterisation are essentially non-volatile for the 100 s  
399 simulation time. Modal compositions  $C_{20}H_{42}$  ( $\sigma = 1$ ),  $C_{19}H_{40}$  ( $\sigma = 2$ ) and  $C_{17}H_{36}$  ( $\sigma = 3$ ) can produce  
400 REPARTEE-like aerosol dynamics.

401

402 Vapour pressure parameterisation B-c has the highest vapour pressure for all compounds in  
403 comparison with Co and A-a. Hence, particles in the nucleation mode are subject to a more  
404 pronounced evaporation, even for modal compositions  $C_{28}H_{58}$  to  $C_{32}H_{66}$ . Nonetheless, only  
405 modal compositions  $C_{25}H_{52}$  ( $\sigma = 1$ ),  $C_{24}H_{50}$  ( $\sigma = 2$ ),  $C_{23}H_{48}$  ( $\sigma = 3$ ),  $C_{21}H_{44}$  ( $\sigma = 4$ ) and  $C_{20}H_{42}$  ( $\sigma = 5$ )  
406 are able to produce the REPARTEE-like behaviour. Table 2 provides details on the modal  
407 compositions and composition standard deviations that approximate the REPARTEE-like aerosol  
408 dynamics for B-c, Co and A-a vapour pressure parameterisations.

409

410 The difference in 100-s  $D_{pg,nuc}$  between the highest vapour pressure (B-c) and the lowest vapour  
411 pressure (A-a) for all values of  $\sigma$ , is shown in Figure 6. The largest differences (10-14 nm)  
412 between the  $D_{pg,nuc}$  occur for modal compositions between  $C_{22}H_{46}$  and  $C_{24}H_{50}$  and  $\sigma = 1, 2, 3$ . For  
413 model run-time of 100 s, the variability of the UFP shrinkage due to the uncertainty of vapour  
414 pressure data is highest for the compositions between  $C_{22}H_{46}$  and  $C_{24}H_{50}$ . From Figure 3, we see

31  
32



415 that the uncertainty of vapour pressure data increases monotonically with carbon number and  
416 is highest for  $C_{32}H_{66}$ . However this high level of uncertainty for high-carbon compositions does  
417 not exert a significant impact on the model results. We thus conclude that the accuracy of  
418 vapour pressure values for very high or very low carbon compositions are not important for  
419 neighbourhood-scale aerosol dynamics.

420

### 421 **3.3 Effect of Non-Volatile Core on the Nucleation Mode Peak Particle Diameter**

422 To consider how the fraction of non-volatile core interacts with the SVOCs composition and the  
423 vapour pressure parameterisations, we define a '100-s effective non-volatile core': the  
424 nucleation mode peak diameter at 100 s of evaporation. Figure 7 shows results for three non-  
425 volatile fractions (initial 1%, 5% and 10% based on mass) and vapour pressures A-a, B-c and Co  
426 (cf. Figure 3), for a modal composition of  $C_{16}H_{34}$ . Results for the remaining modal compositions  
427 are not plotted here because using modal composition  $C_{16}H_{34}$  and an evaporation time of 100 s  
428 gives the maximum reduction of the nucleation-mode peak diameter for all  $\sigma$  in our model runs.  
429 However, we show the results for modal compositions  $C_{24}H_{50}$  and  $C_{32}H_{66}$  for completeness in the  
430 Supplementary Information (Figure 7-S).

431

432 Because the mass-size distribution is held constant for each model initialisation (see  
433 Supplementary Information), an increase of the non-volatile material in the nucleation mode  
434 leads to a decrease in the total amount of n-alkane SVOC available for evaporation, and hence  
435 leads to an increase in the nucleation mode 'dry' (i.e. non-volatile core only) diameter from  $\sim 9$   
436 nm to  $\sim 12$  nm. For the lowest volatility parameterisation (A-a), only the lightest surrogate  
437 compounds near  $C_{16}H_{34}$  are sufficiently volatile over the timescale of the model run to drive  
438 evaporation of nucleation mode particles. As  $\sigma$  increases, an increasing number of lower  
439 volatility components are added into the particle composition, causing the 100-s effective non-  
440 volatile core to increase.

441

33

34

442 Considering REPARTEE-like behaviour, i.e., shrinkage of the nucleation mode diameter to ca. 10  
443 nm, initial non-volatile core fractions of 5% or greater do not reproduce the observed  
444 behaviour.

445

446

#### 447 **4. DISCUSSION AND CONCLUSIONS**

448 The purpose of this study was to evaluate the importance of particle composition and saturation  
449 vapour pressure on the evolution of urban ultrafine diesel particles on the neighbourhood scale  
450 ( $\ll 1$  km) by means of numerical simulations. We present the effect of evaporation on the size-  
451 resolved ultrafine particles and looked at the evolution of the nucleation-mode peak diameter  
452  $D_{pg,nuc}$  depending on particle SVOC composition, vapour pressure, and fraction of non-volatile  
453 core in the particles. We have used laboratory measurements of the size-resolved composition  
454 of the ultrafine particles as an additional strong constraint on the plausibility of model  
455 parameter sets. We identified a group of surrogate n-alkane compounds in the range  $C_{16}H_{34}$ -  
456  $C_{32}H_{66}$  that could explain REPARTEE-like aerosol dynamics measured in London (Dall'Osto et al.,  
457 2011): i.e., a final nucleation-mode peak diameter at 10 nm or below when particles were  
458 subject to evaporation in a timescale of 100 s. Table 2 highlighted the set of parameters in terms  
459 of vapour pressure and modal compositions that produce such REPARTEE-like behaviour.

460

461 Table 2 presents the sets of model parameters consistent with diameter reduction due to  
462 evaporation. The question remains, however, to what extent these results are realistic and  
463 relevant for the real-world atmosphere. Standard deviation  $\sigma = 1$  for all vapour pressures  
464 narrows significantly the contribution from the n-alkanes ( $[\max(16, j-2):\min(32, j+2)]$  for modal  
465 composition  $j$ ), present in the initial composition of the nucleation mode particles. At  $\sigma = 2$ , the  
466 main contributing compounds involved in particle composition are the modal composition  $j$  and  
467 the surrogate molecules  $[\max(16, j-4):\min(32, j+4)]$ . This means that for the given vapour  
468 pressure parameterisation, A-a, and modal composition  $C_{19}H_{40}$ , the compounds found in the

35

36

469 particles would be between  $C_{15}H_{32}$  and  $C_{23}H_{48}$ . However,  $C_{16}H_{34}$  is the lower limit of surrogate  
470 compounds in the model, so the Gaussian distribution of composition is truncated at the low-  
471 carbon-number end in this case. At  $\sigma = 3$ , the contributing compounds found in the particles are  
472 the surrogate molecules in the range  $[\max(16, j-7): \min(32, j+7)]$ . For a modal composition  $C_{17}H_{36}$   
473 and A-a vapour pressure, the range of participating compounds is  $C_{16}H_{34}$ - $C_{24}H_{50}$ , similar to the  
474 case of  $\sigma = 2$ . At  $\sigma = 4$  and 5, the majority of the surrogate molecules in our range of n-alkanes  
475 participate in the composition of particles, thus providing a reasonable range over the  
476 contribution from diesel fuel and engine lubricating oil. The range at  $\sigma = 3$  could be considered  
477 as a transition range, while examples at  $\sigma = 2$  would have compositions that are rather more  
478 limited than available measurements in the Aitken mode (e.g. Figure 1), with a focus on the  
479 contribution from the engine lubricating oil. Overall, narrow compositions would imply a strong  
480 gradient of SVOCs across the nucleation and Aitken modes whereas broad compositions imply  
481 that SVOCs are more or less evenly distributed across the ultrafine size range.

482 Table 3 shows an additionally constrained range of modal compositions consistent with what we  
483 know from field and laboratory measurements combined. The lowest vapour pressure  
484 parameterisations (A-a and the very similar B-a, see Figure 3) are less likely, at any modal  
485 composition standard deviation ( $\sigma$ ), to represent the laboratory and field observations together.  
486 The results reported in Alam et al. (2016) and in Figure 1 show that diesel ultrafine particle  
487 emissions are composed of a wealth of SVOCs that are mainly identified as straight and  
488 branched alkanes in the range  $C_{11}$ - $C_{33}$ , cycloalkanes ( $C_{11}$ - $C_{25}$ ), PAHs, various cyclic aromatics,  
489 alkyl benzenes and decalins. They report emitted particulate size fractionated concentrations of  
490 n-alkanes (cf. Figure 2-S in Supplementary Information) and point out that particles in the 5-  
491 100nm diameter range consist mainly of high molecular weight SVOCs ( $>C_{24}H_{50}$ ) associated with  
492 engine lubricating oil. The work of Robinson et al. (2007), Grishop et al. (2009) and May et al.  
493 (2013) also point to a Gaussian-type distribution of the exhaust particle composition centred at  
494 SVOC, that has a wide standard deviation.

496

497 Vapour pressure parameterisations used in this study and plotted in Figure 3, are one of the  
498 crucial input parameters in assessing the rate at which condensation/evaporation can occur,  
499 though they are poorly constrained. We introduced a new concept of threshold modal  
500 composition, i.e. modal composition that is not sensitive to  $\sigma$  for a given model output time. In  
501 an order of decreasing vapour pressure (Figure 3) and timescale of 100 s, the threshold modal  
502 composition value changes from  $C_{27}H_{56}$  for the B-c parameterisation (Figure 4-S, Supplementary  
503 Information), to  $C_{25}H_{52}$  for Co (Figure 5), to  $C_{22}H_{46}$  for A-a (Figure 5-S, Supplementary  
504 Information). Overall, the largest differences ( $\sim 14$  nm) in the 100-s  $D_{pg,nuc}$  occur between the  
505 highest (B-c) and the lowest (A-a) vapour pressure parameterisations for modal compositions  
506 between  $C_{22}H_{46}$  and  $C_{24}H_{50}$  and composition standard deviation from 1 to 3. The vapour  
507 pressures of components in this range are therefore critical for the modelling of nucleation-  
508 mode aerosol dynamics on the neighbourhood scale. For components with volatility less than  
509 that for the  $C_{22}H_{46}$  surrogate compound used here, all available vapour pressure  
510 parameterisations render these compounds volatile over the 100-s timescale. These  
511 components will equilibrate with the gas phase on these short timescales. Components with  
512 volatility lower than that of the  $C_{24}H_{50}$  surrogate are effectively non-volatile over this timescale  
513 for all vapour pressure parameterisations, and so will remain condensed and out-of-equilibrium  
514 with the gas phase on these timescales.

515

516 The other variable which will influence evaporation rate is the concentration of vapour  
517 surrounding the particles. In this work, measured roadside vapour concentrations reported by  
518 Harrad et al. (2003) are used (see also Nikolova et al., 2016). These represent an upper estimate  
519 of gas-phase partial pressures away from roadside. Mixing of cleaner urban background air into  
520 the simulated air parcel would lower partial pressures and increase evaporation rates.

521

522 The 100-s effective non-volatile core (the nucleation mode peak diameter at 100 s of

39

40

523 evaporation) increased from ~9 nm to ~12 nm. This was attributed to the decrease in the total  
524 amount of n-alkane surrogate compounds present for evaporation. As composition standard  
525 deviation  $\sigma$  increased, an increasing number of lower volatility components added into the  
526 particle composition caused the 100-s effective non-volatile core to further increase.

527 Considering REPARTEE-like behaviour, i.e., shrinkage of the nucleation mode diameter to ca. 10  
528 nm, an initial non-volatile core of 5% by mass or greater was not capable of reproducing the  
529 observed behaviour in the atmosphere. Because the higher molecular weight (lower volatility)  
530 surrogate molecules in the model are essentially non-volatile over the modelling timescale, the  
531 nucleation mode dynamics due to SVOC is confounded with that due to the size of any non-  
532 volatile core present in the particles.

533

534 Results (Figure 7) suggest that urban nucleation mode particles should be predominantly  
535 volatile in order to produce REPARTEE-like behaviour. In these numerical experiments, the  
536 nature of the non-volatile core need not be specified. This core could be composed of one or  
537 more low vapour pressure compounds, not affected by condensation/evaporation on the  
538 timescale of the model and measurements. On the other hand, as discussed in Nikolova et al.  
539 (2016), a non-volatile core could be composed mainly of carbon and possibly some contribution  
540 from metal oxides and sulphates. This difference in composition could be relevant to effects on  
541 human health. Li et al. (2010) show that diesel truck emissions during idle induce a high level of  
542 oxidative stress in human aortic endothelial cells, due to the type of metals and trace metals  
543 found in the exhaust, while Xia et al. (2015) argue that traffic-related UFP act to promote airway  
544 inflammation due to the rich content of organic species. The relative importance of these  
545 particles in affecting human health merits further investigations.

546

547 Laboratory exhaust diesel ultrafine particulate measurements are highly dependent on the  
548 sampling methods. Measurements of the ultrafine particle composition from a diesel-fuelled  
549 engine are still at an early stage and therefore more efforts should be put into developing

41

42

550 sampling protocols that target the composition of the nucleation and Aitken modes particles in  
551 a realistic manner. There are no robust UFP chemical composition measurements at street scale  
552 and therefore such measurements devoted to address in detail the composition of the traffic  
553 emitted UFP in the atmosphere are urgently needed. Saturation vapour pressure is another  
554 source of large uncertainties; our study lays out a strategy to determine which vapour pressures  
555 are most significant in a given modelling scenario.

556

557

## 558 **ACKNOWLEDGEMENTS**

559 This work is part of the FASTER project, ERC-2012-AdG, Proposal No. 320821 sponsored by the  
560 European Research Council (ERC).

561

## 562 **REFERENCES**

563 Alam, M. S, Rezaei, S. Z., Stark, C. P., Liang, Z., Xu, H. M. and Harrison, R. M.: The  
564 characterisation of diesel exhaust particles – composition, size distribution and partitioning,  
565 Faraday Discuss., 189, 69-84, 2016.

566

567 Alam, M. S., Liang, Z., Rezaei, S. Z., Stark, C. P., Xu, H. M., MacKenzie, A. R. and Harrison, R. M.:  
568 Mapping and quantifying isomer sets of hydrocarbons ( $\geq C_{12}$ ) in diesel fuel, lubricating oil and  
569 diesel exhaust samples using GC $\times$ GC-ToFMS, Atmos. Meas. Tech. Discuss., submitted, 2017.

570

571 Allen, L. R., Donahue, N. M., Shrivastava, M. K., Weitkamp, E. A., Sage, A. M., Grieshop, A. P.,  
572 Lane, T. E., Pierce, J. R. and Pandis, S. N.: Rethinking organic aerosols: semivolatile emissions and  
573 photochemical aging. Science, 315, 1259-62, 2007.

574

575 Atkinson, R. W., Fuller, G. W., Anderson, H. R., Harrison, R. M. and Armstrong, B.: Urban  
576 ambient particle metrics and health: a time-series analysis, Epidemiology, 21, 501-511, 2010.

43

44

577

578 Biswas, S., Ntziachristos, L., Moore, K. F. and Sioutas, C: Particle volatility in the vicinity of a  
579 freeway with heavy-duty diesel traffic, *Atmos. Environ.*, 41, 3479-3493, 2007.

580

581 Chan, A. W. H., Isaacman, G., Wilson, K. R., Worton, D. R., Ruehl, C. R., Nah, T., Gentner, D. R.,  
582 Dallmann, T. R., Kirchstetter, T. W., Harley, R. A., Gilman, J. B., Kuster, W. C., de Gouw, J. A.,  
583 Offenberg, J. H., Kleindienst, T. E., Lin, Y. H., Rubitschun, C. L., Surratt, J. D., Hayes, P. L., Jimenez,  
584 J. L. and Goldstein, A. H.: Detailed chemical characterization of unresolved complex mixtures in  
585 atmospheric organics: insights into emission sources, atmospheric processing, and secondary  
586 organic aerosol formation, *J. Geophys. Res.: Atmospheres*, 118, 6783-6796, 2013.

587

588 Chickos, J. and Lipkind, D.: Hypothetical thermodynamic properties: vapour pressures and  
589 vaporization enthalpies of the even n-Alkanes from C78 to C92 at T= 298.15K by correlation-gas  
590 chromatography, *J. Chem. Eng. Data*, 53, 2432-2440, 2008.

591

592 Compernelle, S., Ceulemans, K. and Muller, J. -F.: Evaporation: a new vapour pressure  
593 estimation method for organic molecules including non-additivity and intramolecular  
594 interactions, *Atmos. Chem. Phys.*, 11, 9431-9450, 2011.

595

596 Dall'Osto, M., Thorpe, A., Beddows, D.C.S., Harrison, R.M., Barlow, J.F., Dunbar, T., Williams, P.I.  
597 and Coe, H.: Remarkable dynamics of nanoparticles in the urban atmosphere, *Atmos. Chem.*  
598 *Phys.*, 11, 6623-6637, 2011.

599

600 Donahue, N. M., Robinson, A. L., Stanier, C. O., and Pandis, S. N.: Coupled partitioning, dilution,  
601 and chemical aging of semivolatile organics, *Environ. Sci. Technol.*, 40, 2635-2643,  
602 2006.

603

45

46

604 Grieshop, A., Miracolo, M., Donahue, N., and Robinson, A.: Constraining the volatility  
605 distribution and gas-particle partitioning of combustion aerosols using isothermal dilution and  
606 thermodenuder measurements., *Environ. Sci. Technol.*, 43, 4750, 2009.

607

608 Harrad, S., Hassoun, S., Callen Romero, M.S. and Harrison, R.M.: Characterisation and source  
609 attribution of the semi-volatile organic content of atmospheric particles and associate  
610 vapour phase in Birmingham, UK, *Atmos. Environ.*, 37, 4985-4991, 2003.

611

612 Harrison, R. M., Beddows, D. S. and Dall'Osto, M.: PMF analysis of wide-range particle size  
613 spectra collected on a major highway, *Environ. Sci. Technol.*, 45, 5522-5528, 2011.

614

615 Harrison, R. M., Dall'Osto, M., Beddows, D. C. S., Thorpe, A. J., Bloss, W. J., Allan, J. D., Coe, H.,  
616 Dorsey, J. R., Gallagher, M., Martin, C., Whitehead, J., Williams, P. I., Jones, R. L., Langridge, J.  
617 M., Benton, A. K., Ball, S. M., Langford, B., Hewitt, C. N., Davison, B., Martin, D., Petersson, K. F.,  
618 Henshaw, S. J., White, I. R., Shallcross, D. E., Barlow, J. F., Dunbar, T., Davies, F., Nemitz, E.,  
619 Phillips, G. J., Helfter, C., Di Marco C. F. and Smith, S.: Atmospheric chemistry and physics in the  
620 atmosphere of a developed megacity (London): an overview of the REPARTEE experiment and  
621 its conclusions, *Atmos. Chem. Phys.*, 12, 3065-3114, 2012.

622

623 Harrison, R.M., Jones, A.M., Beddows, D.C.S., Dall'Osto M. and Nikolova, I.: Evaporation of  
624 traffic-generated nanoparticles during advection from source, *Atmos. Environ.*, 125, 1-7, 2016.

625

626 Joback, K. and Reid, R.: Estimation of Pure-component properties from group-contributions,  
627 *Chem. Eng. Commun.*, 57, 233-243, 1987.

628

629 Jacobson, M.Z.: Development and application of a new air pollution modeling system. 2. Aerosol  
630 module structure and design, *Atmos. Environ.*, 31, 131-144, 1997.



631

632 Jacobson, M. Z., Kittelson, D. B., and Watts, W. F.: Enhanced coagulation due to evaporation and  
633 its effect on nanoparticle evolution, *Environ. Sci. Technol.*, 39, 9486- 9492, 2005.

634

635 Julin, J., Winkler, P. M., Donahue, N. M., Wagner, P. E. and Riipinen, I.: Near-unity mass  
636 accommodation coefficient of organic molecules of varying structure, *Environ. Sci. Technol.*, 48,  
637 12083-12089, 2014.

638

639 Karl, M., Kukkonen, J., Keuken, M. P., Lützenkirchen, S., Pirjola, L., and Hussein, T.: Modeling and  
640 measurements of urban aerosol processes on the neighborhood scale in Rotterdam, Oslo and  
641 Helsinki, *Atmos. Chem. Phys.*, 16, 4817-4835, doi:10.5194/acp16-4817-2016, 2016.

642

643 Karnezi, E., Riipinen, I. and Pandis, S. N.: Measuring the atmospheric organic aerosol volatility  
644 distribution: a theoretical analysis, *Atmos. Meas. Tech. Discuss.*, 7, 2953-2965, 2014.

645

646 Kumar, P., Morawska, L., Birmili, W., Paasonen, P., Hu, M., Kulmala, M., Harrison, R. M., Norford,  
647 L. and Britter, R.: Ultrafine particles in cities, *Environ. Intl.*, 66, 1-10, 2014.

648

649 Lemmon, E. W. and Goodwin, A. R. H.: Critical properties and vapour pressure equation for  
650 alkanes  $C_nH_{2n+2}$ : normal alkanes with  $n \leq 36$  and isomers for  $n = 4$  through  $n = 9$ , *J. Phys. Chem.*  
651 *Ref. Data*, 29, 1-39, 2000.

652

653 Li, R., Ning, Z., Majumdar, R., Cui, J., Takabe, W., Jen, N., Sioutas, C. and Hsiai, T.: Ultrafine  
654 particles from diesel vehicle emissions at different driving cycles induce differential vascular pro-  
655 inflammatory responses: implications of chemical components and NF- $\kappa$ B signaling, *Part. Fibre*  
656 *Toxicol.*, 7-6, 2010.

657

49

50

658 May, A. A., Presto, A. A., Hennigan, C. J., Nguyen, N. T., Gordon, T. D., and Robinson, A. L.: Gas-  
659 particle partitioning of primary organic aerosol emissions: (2) Diesel vehicles, *Environ. Sci.*  
660 *Technol.*, 47, 8288-8296, 2013.

661

662 Myrdal, P. B. and Yalkowsky, S. H.: Estimating pure component vapor pressures of complex  
663 organic molecules, *Ind. Eng. Chem. Res.*, 36, 2494-2499, 1997.

664

665 Nannoolal, Y., Rarey, J., Ramjugernath, D. and Cordes, W.: Estimation of pure component  
666 properties: Part 1. Estimation of the normal boiling point of non-electrolyte organic compounds  
667 via  
668 group contributions and group interactions, *Fluid Phase Equilibr.*, 226, 45-63, 2004.

669

670 Nannoolal, Y., Rarey, J. and Ramjugernath, D.: Estimation of pure component properties: Part 3.  
671 Estimation of the vapor pressure of non-electrolyte organic compounds via group contributions  
672 and group interactions, *Fluid Phase Equilibr.*, 269, 117-133, 2008.

673

674 Nikolova, I., Janssen S., Vos, P., Vrancken, K., Mishra, V. and Berghmans, P.: Dispersion  
675 modelling of traffic induced ultrafine particles in a street canyon in Antwerp, Belgium and  
676 comparison with observations, *Sci. Total Environ.*, 412-413, 336-43, 2011.

677

678 Nikolova, I., MacKenzie, A. R., Cai, X., Alam, M. S. and Harrison, R. M.: Modelling component  
679 evaporation and composition change of traffic-induced ultrafine particles during travel from street  
680 canyon to urban background, *Faraday Discuss.*, 189, 529-546, 2016.

681

682 Pugh, T. A. M., MacKenzie, A. R., Whyatt, J. D. and Hewitt, C. N.: Effectiveness of green  
683 infrastructure for improvement of air quality in urban street canyons, *Environ. Sci. Technol.*, 46,  
684 7692-7699, 2012.

685

686 Robinson, A. L., Donahue, N. M., Shrivastava, M. K., Weitkamp, E. A., Sage, A. M., Grieshop, A.  
687 P., Lane, T. E., Pierce, J. R. and Pandis, S. N.: Rethinking organic aerosols: semivolatile emissions  
688 and photochemical aging, *Science*, 315, 1259-1262, 2007.

689

690 Ronkko, T., Lahde, T., Heikkila, J., Pirjola, L., Bauschke, U., Arnold, F., Schager, H., Rothe, D., Yli-  
691 Ojanpera, J. and Keskinen, J.: Effects of Gaseous Sulphuric Acid on Diesel Exhaust Nanoparticle  
692 Formation and Characteristics, *Environ. Sci. Technol.*, 47, 11882-11889, 2013.

693

694 Stein, S. E. and Brown, R. L.: Estimation of normal boiling points from group contributions, *J.*  
695 *Chem. Inf. Comp. Sci.*, 34, 581-58, 1994.

696

697 Topping, D., Barley, M., Bane, M. K., Higham, N., Aumont, B., Dingle, N., and McFiggans, G.:  
698 UManSysProp v1.0: an online and open-source facility for molecular property prediction and  
699 atmospheric aerosol calculations, *Geosci. Model Dev.*, 9, 899-914, 2016.

700

701 US EPA: Estimation Programs Interface Suite™ for Microsoft® Windows, v 4.11, United States  
702 Environmental Protection Agency, Washington, DC, USA, 2017.

703

704 Wehner, B., Philippin, S., Wiedensohler, A., Scheer, V. and Vogt, R.: Variability of non-volatile  
705 fractions of atmospheric aerosol particles with traffic influence, *Atmos. Environ.*, 38, 6081-6090,  
706 2004.

707

708 Xia, M., Viera-Hutchins, L., Garcia-Lloret, M., Rivas, M. N., Wise, P., McGhee, S. A., Chatila, Z. K.,  
709 Daher, N., Sioutas, C. and Chatila, T. A.: Vehicular exhaust particles promote allergic airway  
710 inflammation through an aryl hydrocarbon receptor-notch signaling cascade, *J. Allergy Clin.*  
711 *Immun.*, 136, 441-453, 2015.

53

54

713 **TABLE LEGENDS**

714 **Table 1.** Total mass  $M$  ( $\text{ng m}^{-3}$ ) of nucleation mode peak particles at 1 s and 100 s of  
 715 simulation for modal compositions  $\text{C}_{16}\text{H}_{34}$ - $\text{C}_{32}\text{H}_{66}$  and composition standard  
 716 deviations,  $\sigma$ . For comparison, the initial mass of the non-volatile material in the  
 717 nucleation mode peak particles is  $2.9 \text{ ng m}^{-3}$ .

718

719 **Table 2.** Modal composition ranges and composition standard deviations,  $\sigma$ , producing  
 720 model results that approximate REPARTEE-like behaviour (see main text), for  
 721 different vapour pressure parameterisations. Initial non-volatile core in the nucleation  
 722 mode is set to 1%.

723

724 **Table 3.** Modal composition range and composition standard deviations,  $\sigma$ , producing  
 725 more realistic results that approximate REPARTEE-like behaviour. Vapour pressure  
 726 parameterisation follows Myrdal and Yalkowski (1997; B-c in Figure 3),  
 727 Compernelle et al. (2011; Co in Figure 3), and Nannoolal 2008; A-a in Figure 3).  
 728 Column 'cn' indicates the carbon number of compounds  $n$  in the modal composition  
 729 with a contribution bigger than 1%.

730

731

732 **FIGURE LEGENDS**

733 **Figure 1.** A GC $\times$ GC chromatogram (contour plot) indicating homologous series of compounds  
 734 identified in diesel engine exhaust emissions. Emissions from a light-duty diesel  
 735 engine operating at 1800 revolutions per minute and 1.4 bar brake mean effective  
 736 pressure. Compounds identified in the contour plot are indicated by the coloured  
 737 polygons – Lower black polygons are  $n$ - +  $i$ -alkanes; red polygons are monocyclic  
 738 alkanes; green polygons are bicyclic alkanes; pink polygons are aldehydes + ketones;  
 739 and upper black polygons are monocyclic aromatics. Each peak in the contour plot

740 represents a compound present in the emissions; warmer colours (e.g. red) are more  
741 intense peaks while colder colours (blue) are smaller peaks. Contour plot were  
742 produced by GC Image v2.5. Bar charts above show the volatility distribution of total  
743 alkanes (red) and total identified species (black), indicating that the majority of the  
744 emissions consist of alkanes. For details of the compound attribution method, see  
745 Alam et al. (2017).

746

747 **Figure 2.** An example of nucleation mode UFP compositions, represented as mass fractions for  
748 surrogate compounds  $C_nH_{(2n+2)}$ ,  $n = [16:32]$ , and described by a Gaussian distribution  
749 centred on  $C_{24}H_{50}$  with standard deviation,  $\sigma$ , from 1 to 5.

750

751 **Figure 3.** Vapour pressure data for selected n-alkanes  $C_nH_{(2n+2)}$  where  $n = [16:32]$  at 298K.  
752 Abbreviations in the legend point to the source as follows: A and B refer to the  
753 vapour pressure data from Nannoolal et al. (2008) and Myrdal and Yalkowsky  
754 (1997), respectively; -a, -b and -c refer to the boiling point of Joback and Reid  
755 (1987), Stein and Brown (1994) and Nannoolal et al. (2004), respectively; ES refers  
756 to Epi Suite calculator (U.S. Environmental Protection Agency); Co to Compernelle  
757 et al. (2011); Ch to Chickos and Lipkind (2008), LG to Lemmon and Goodwin  
758 (2000).

759

760 **Figure 4.** Nucleation mode peak diameter  $D_p$  [nm] at 1 s of simulation depending on the modal  
761 composition and the composition standard deviation. The initial nucleation mode  
762 peak diameter is at 23nm (not shown on the figure). Vapour pressure data follows  
763 Compernelle et al. (2011).

764

765 **Figure 5.** Nucleation mode peak diameter  $D_p$  [nm] at 100 s of simulation depending on the  
766 modal composition and the composition standard deviation. The initial nucleation

767 mode peak diameter is at 23nm (not shown on the figure). Vapour pressure data

768 follows Compernelle et al. (2011).

769

770 **Figure 6.**  $D_{pg,nuc}$  difference between the nucleation mode peak diameter (nm) when using B-c

771 vapour pressure and the nucleation mode peak diameter when using A-a vapour

772 pressure for modal compositions  $C_nH_{(2n+2)}$  where  $n = [16:32]$ .

773

774 **Figure 7.** Nucleation mode peak diameter  $D_p$  [nm] at 100 s: the ‘100-s effective non-volatile

775 core’ for the nucleation mode. Results are shown at 1%, 5% and 10% initial non-

776 volatile material in the nucleation mode particles, modal composition  $C_{16}H_{34}$  and for

777 various composition standard deviations.

778

779

780

781

782

783

784

785

786

787

788

789

790

791	1s																		
792	Centre @	C <sub>16</sub> H <sub>34</sub>	C <sub>17</sub> H <sub>36</sub>	C <sub>18</sub> H <sub>38</sub>	C <sub>19</sub> H <sub>40</sub>	C <sub>20</sub> H <sub>42</sub>	C <sub>21</sub> H <sub>44</sub>	C <sub>22</sub> H <sub>46</sub>	C <sub>23</sub> H <sub>48</sub>	C <sub>24</sub> H <sub>50</sub>	C <sub>25</sub> H <sub>52</sub>	C <sub>26</sub> H <sub>54</sub>	C <sub>27</sub> H <sub>56</sub>	C <sub>28</sub> H <sub>58</sub>	C <sub>29</sub> H <sub>60</sub>	C <sub>30</sub> H <sub>62</sub>	C <sub>31</sub> H <sub>64</sub>	C <sub>32</sub> H <sub>66</sub>	
	Sigma																		
	1	2.9	2.9	2.9	2.9	7.4	23.6	38.1	46.8	51.0	52.6	53.2	53.4	53.4	53.5	53.5	53.5	53.5	53.5
	2	2.9	2.9	3.2	6.9	14.3	24.1	34.0	42.1	47.0	50.3	52.1	52.9	53.3	53.4	53.4	53.5	53.5	53.5
793	3	3.7	5.4	8.4	12.9	18.5	24.9	31.6	38.1	43.5	46.8	49.3	51.0	52.1	52.8	53.1	53.3	53.4	53.4
	4	8.0	10.6	13.7	17.6	21.8	26.4	31.0	35.4	39.7	43.7	46.2	48.2	49.8	50.9	51.8	52.3	52.7	52.7
794	5	12.8	15.3	18.1	21.1	24.4	27.7	31.2	34.4	37.6	40.2	43.0	45.4	47.0	48.4	49.5	50.4	51.2	51.2
	100s																		
795	Centre @																		
	Sigma																		
796	1	2.9	2.9	2.9	2.9	2.9	2.9	2.9	2.9	6.1	23.8	38.9	47.5	51.3	52.8	53.3	53.5	53.6	53.6
	2	2.9	2.9	2.9	2.9	2.9	2.9	3.0	6.2	14.3	24.8	34.8	42.5	47.6	50.6	52.1	52.9	53.2	53.2
	3	2.9	2.9	2.9	2.9	3.1	4.2	7.1	11.9	18.2	25.2	31.9	37.8	42.6	46.1	48.6	50.3	51.4	51.4
797	4	2.9	3.0	3.3	4.1	5.6	7.9	11.1	15.1	19.7	24.6	29.3	33.8	37.7	41.1	43.8	46.1	47.8	47.8
	5	3.7	4.4	5.4	6.9	8.7	11.1	13.8	17.0	20.2	23.7	27.2	30.6	33.7	36.6	39.2	41.4	43.4	43.4

798

799

800 **Table 1.** Total mass M (ng m<sup>-3</sup>) of nucleation mode peak particles at 1 s and 100 s of simulation

801 for modal compositions C<sub>16</sub>H<sub>34</sub>-C<sub>32</sub>H<sub>66</sub> and composition standard deviations, sigma. For

802 comparison, the initial mass of the non-volatile material in the nucleation mode peak particles is

803 2.9 ng m<sup>-3</sup>.

804

805

806

807

808

809

810

811

812

813

814

815

816

817

61

62

818

	Vapour pressure	B-c	Co	A-a
819	Sigma			
	1	$\leq C_{25}H_{52}$	$\leq C_{23}H_{48}$	$\leq C_{20}H_{42}$
820	2	$\leq C_{24}H_{50}$	$\leq C_{22}H_{46}$	$\leq C_{19}H_{40}$
	3	$\leq C_{23}H_{48}$	$\leq C_{21}H_{44}$	$\leq C_{17}H_{36}$
821	4	$\leq C_{21}H_{44}$	$\leq C_{19}H_{40}$	-
822	5	$\leq C_{20}H_{42}$	$\leq C_{17}H_{36}$	-

823

824 **Table 2.** Modal composition ranges and composition standard deviations, sigma, producing  
825 model results that approximate REPARTEE-like behaviour (see main text), for different vapour  
826 pressure parameterisations. Initial non-volatile core in the nucleation mode is set to 1%.

827

828

829

830

831

832

833

834

835

836

837

838

839

840

841

842

843

844

63

64



	Vapour pressure	B-c	Co	A-a	cn
845	Sigma				-/+
846	1	-	-	-	2
	2	$C_{21}H_{44}-C_{24}H_{50}$	$C_{21}H_{44}-C_{22}H_{46}$	-	4
847	3	$C_{19}H_{40}-C_{23}H_{48}$	$C_{19}H_{40}-C_{21}H_{44}$	-	7
	4	$\leq C_{21}H_{44}$	$\leq C_{19}H_{40}$	-	9
848	5	$\leq C_{20}H_{42}$	$\leq C_{17}H_{36}$	-	11

849

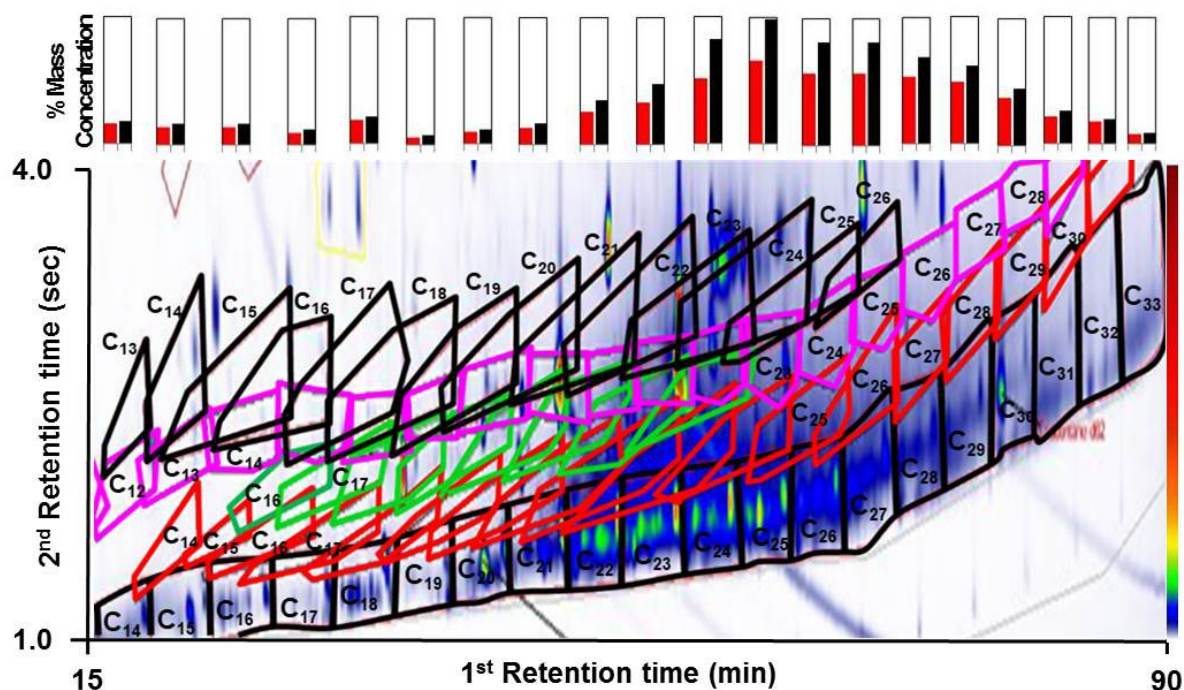
850

851 **Table 3.** Modal composition range and composition standard deviations, sigma, producing more  
852 realistic results that approximate REPARTEE-like behaviour. Vapour pressure parameterisation  
853 follows Myrdal and Yalkowski (1997; B-c in Figure 3), Compernelle et al. (2011; Co in Figure 3),  
854 and Nannoolal et al., 2008; A-a in Figure 3). Column 'cn' indicates the carbon number of  
855 compounds n in the modal composition with a contribution bigger than 1%.

856

857

858



859

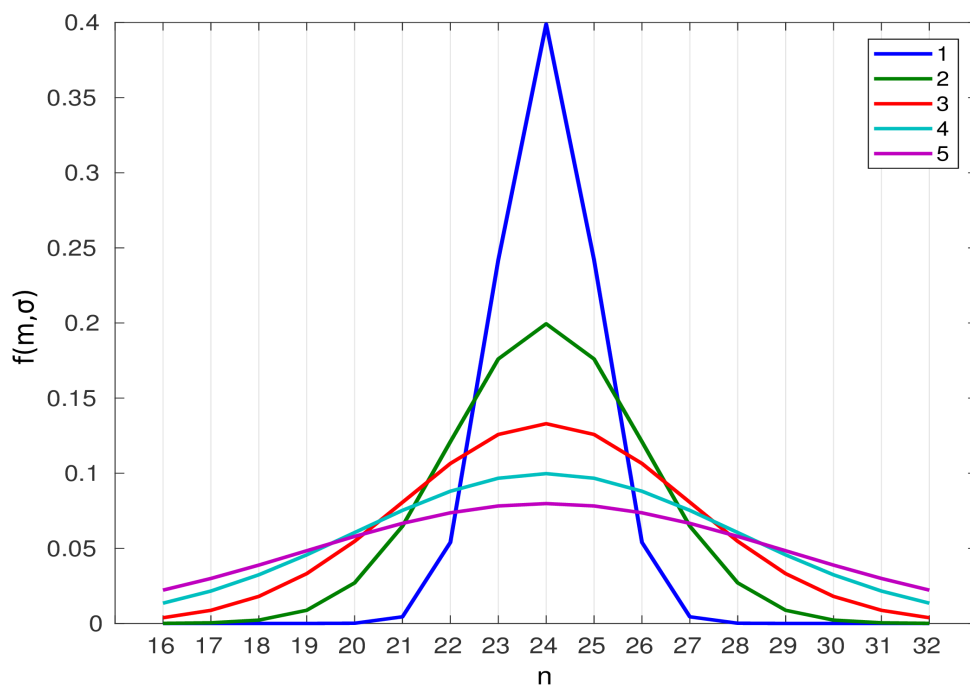
860

861 **Figure 1.** A GCxGC chromatogram (bottom panel, contour plot) indicating homologous series of

65

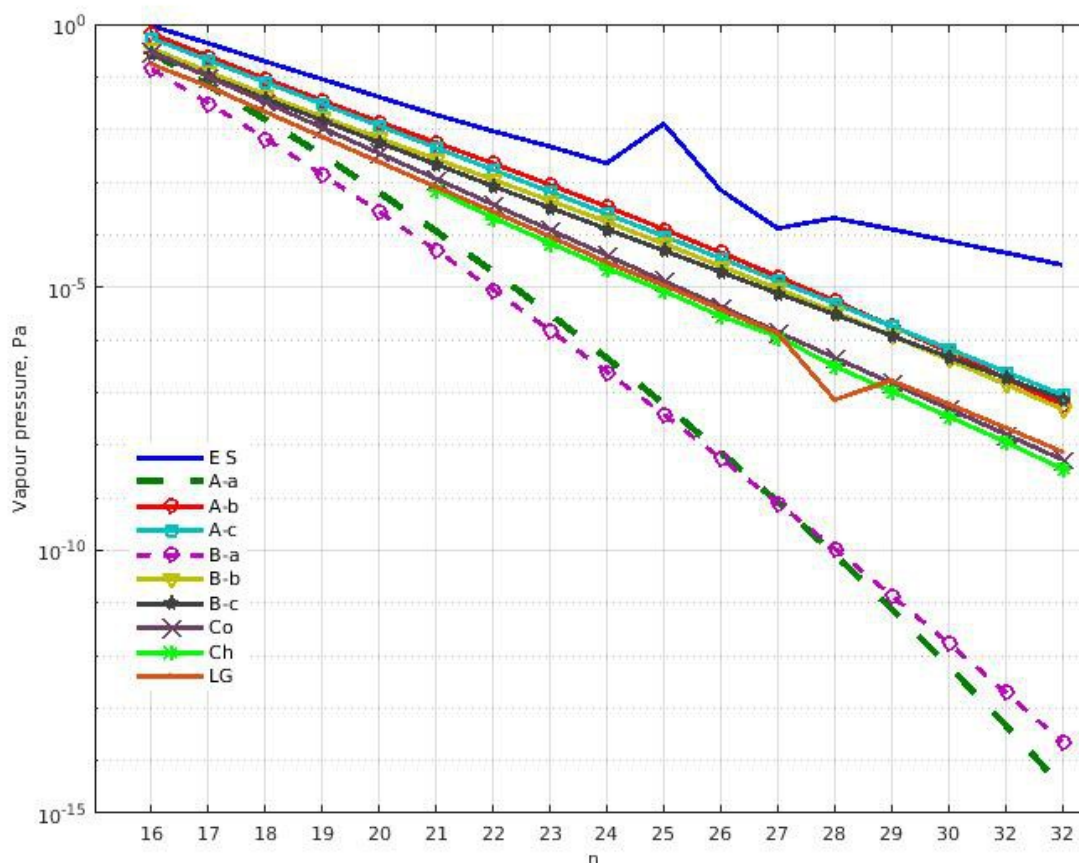
66

862 compounds identified in diesel engine exhaust emissions. Emissions from a light-duty diesel  
863 engine operating at 1800 revolutions per minute and 1.4 bar brake mean effective pressure.  
864 Compounds identified in the contour plot are indicated by the coloured polygons – Lower black  
865 polygons are n- + i-alkanes; red polygons are monocyclic alkanes; green polygons are bicyclic  
866 alkanes; pink polygons are aldehydes + ketones; and upper black polygons are monocyclic  
867 aromatics. Each peak in the contour plot represents a compound present in the emissions;  
868 warmer colours (e.g. red) are more intense peaks while colder colours (blue) are smaller peaks.  
869 Contour plot were produced by GC Image v2.5. Bar chart (top panel) show the volatility  
870 distribution of total alkanes (red) and total identified species (black), indicating that the majority  
871 of the emissions consist of alkanes. For details of the compound attribution method, see Alam  
872 et al. (2017).



888 **Figure 2.** An example of nucleation mode UFP compositions, represented as mass fractions for

889 surrogate compounds  $C_nH_{(2n+2)}$ ,  $n = [16:32]$ , and described by a Gaussian distribution centred on  
 890  $C_{24}H_{50}$  with standard deviation,  $\sigma$ , from 1 to 5.  
 891  
 892  
 893  
 894  
 895  
 896



897  
 898 **Figure 3.** Vapour pressure data for selected n-alkanes  $C_nH_{(2n+2)}$  where  $n = [16:32]$  at 298K.  
 899 Abbreviations in the legend point to the source as follows: A and B refer to the vapour pressure  
 900 data from Nannoolal et al. (2008) and Myrdal and Yalkowsky (1997), respectively; -a, -b and -c  
 901 refer to the boiling point of Joback and Reid (1987), Stein and Brown (1994) and Nannoolal et al.  
 902 (2004), respectively; ES refers to Epi Suite calculator (U.S. Environmental Protection Agency); Co

903 to Compornolle et al. (2011); Ch to Chickos and Lipkind (2008); LG to Lemmon and Goodwin

904 (2000).

905

906

907

908

909

910

911

912

913

914

915

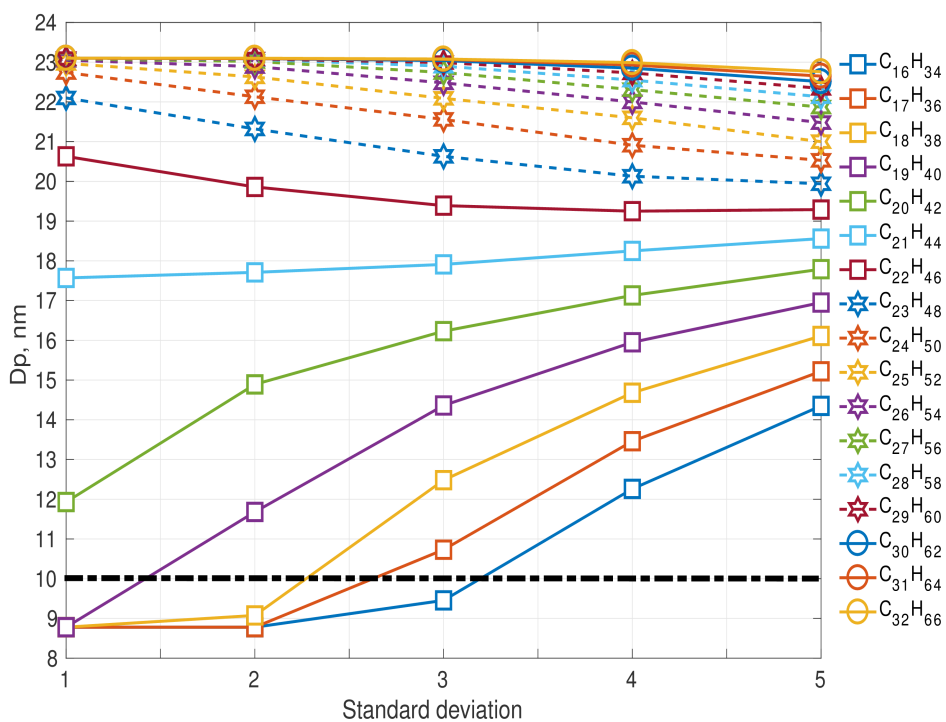
916

917

918

919

920



921

922

923 **Figure 4.** Nucleation mode peak diameter Dp [nm] at 1 s of simulation depending on the modal

924 composition and the composition standard deviation. The initial nucleation mode peak diameter

925 is at 23nm (not shown on the figure). Vapour pressure data follows Compornolle et al. (2011).

926

927

928

929

71

72

930

931

932

933

934

935

936

937

938

939

940

941

942

943

944

945

946

947

948

949

950

951

952

953

954

955

956

73

74

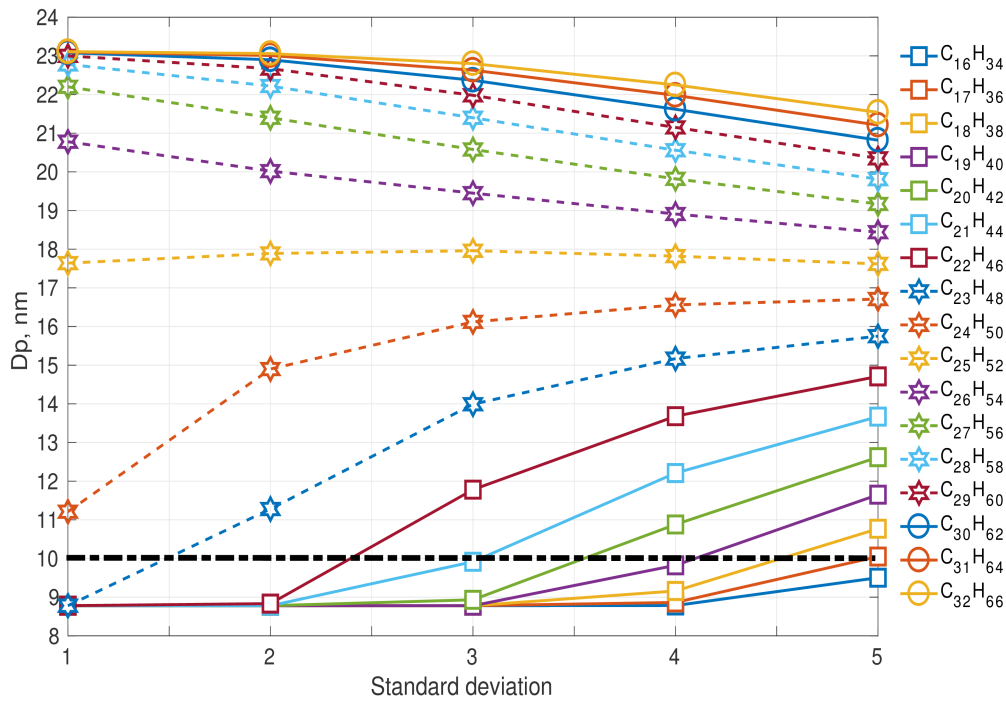


**Figure 5.** Nucleation mode peak diameter  $D_p$  [nm] at 100 s of simulation depending on the modal composition and the composition standard deviation. The initial nucleation mode peak diameter is at 23nm (not shown on the figure). Vapour pressure data follows Compernelle et al. (2011).

957  
958  
959  
960  
961  
962  
963  
964  
965  
966  
967  
968  
969  
970  
971  
972  
973  
974  
975  
976  
977  
978  
979  
980  
981  
982  
983  
75  
76

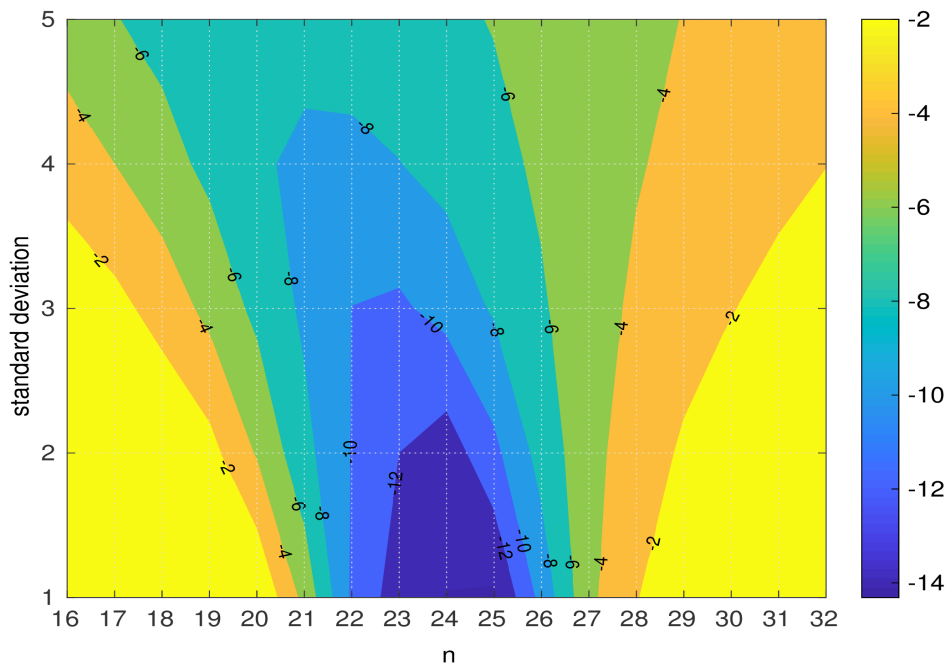


**Figure 6.**  $D_{pg,nuc}$  difference between the nucleation mode peak diameter (nm) when using B-c vapour pressure and the nucleation mode peak diameter when using A-a vapour pressure for modal compositions  $C_nH_{(2n+2)}$  where  $n = [16:32]$ .

984

985

986

987

988

989

990

991

992

993

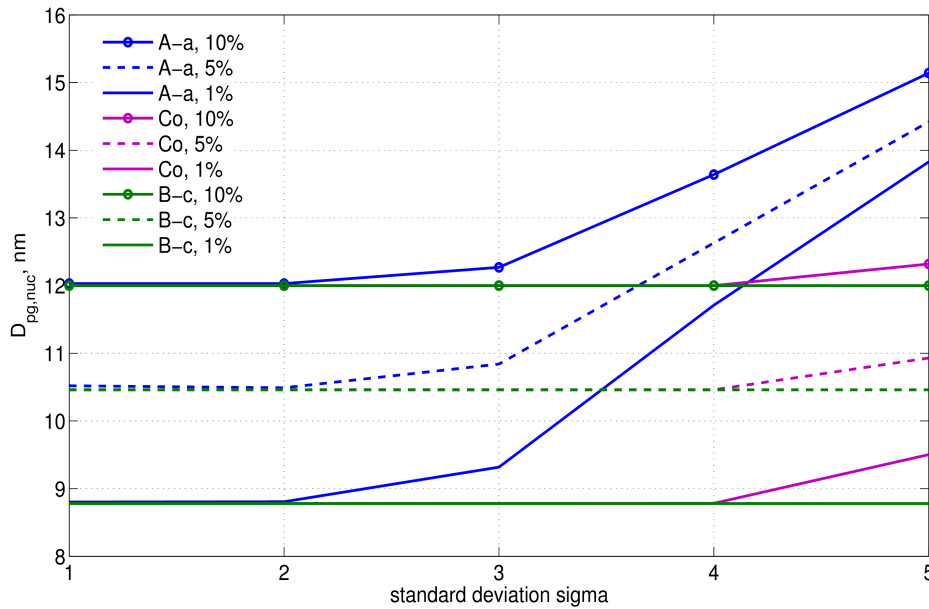
994

995

996

997

998



999 **Figure 7.** Nucleation mode peak diameter  $D_p$  [nm] at 100 s: the '100-s effective non-volatile  
 1000 core' for the nucleation mode. Results are shown at 1%, 5% and 10% initial non-volatile material  
 1001 in the nucleation mode particles, modal composition  $C_{16}H_{34}$  and for various composition  
 1002 standard deviations.

1003